The Cryosphere Discuss., 6, 4695–4731, 2012
www.the-cryosphere-discuss.net/6/4695/2012/
doi:10.5194/tcd-6-4695-2012

The Cryosphere Discussions

Radio-frequency probes of Antarctic ice birefringence at South Pole vs. East Antarctica; evidence for a changing ice fabric

D. Besson[1], N. Doolin[1], M. Stockham[1], and I. Kravchenko[2]

[1]University of Kansas, Dept. of Physics, Lawrence, KS 66045–7582, USA
[2]University of Nebraska, Dept. of Physics, Lincoln, NE 68588–0299, USA

Received: 1 October 2012 – Accepted: 26 October 2012 – Published: 14 November 2012

Correspondence to: D. Besson (zedlam@ku.edu)

Published by Copernicus Publications on behalf of the European Geosciences Union.

Abstract

Following pioneering efforts in East Antarctica, we herein report on the amplitude and temporal characteristics of polarized surface radar echo data collected in South Polar ice using radio sounding equipment with 0.5-ns echo-time precision. We observe strong echoes at 6, 9.6, 13.9, 17, and 19 µs following vertical pulse emission from the surface, in the upper half of the ice sheet. The synchronicity of those echoes for all broadcast azimuthal polarizations affirms the lack of observable birefringence over the upper half of the ice sheet, in contrast to East Antarctica measurements in the vicinity of Dome Fuji, and signifies a dramatic difference in the character of the ice sheet in the intervening 1400 km. Of the five strongest echoes, three exhibit an evident correlation with the local surface ice flow direction, qualitatively consistent with measurements in East Antarctica. Our radio sounding measurements also permit the most precise determination to date of the ice thickness at South Pole.

1 Introduction

In the current picture, radio frequency scattering is primarily the result of three different mechanisms as one probes from the ice surface down to the bed. In the uppermost portion of the ice sheet, scattering is dominated by layered density variations, followed by so-called “acid”, or “conductivity” scattering (sulfates and nitrate layers, e.g. often associated with volcanic activity), followed by “crystal orientation fabric” (COF) scattering due to changes in the crystal orientation in the deeper ice, presumably resulting from a combination of considerable overpressure and the resistance to motion presented by the underlying bedrock. Near the bed is an “echo-free zone” (EFZ), in which the reflection strengths are typically smaller than current instrumental sensitivity (Drews et al., 2009). The three scattering types can be separated on the basis of the magnitude of the radar echoes they produce, as well as the frequency dependence of those radar echoes. The most extensive (and, to a large extent, defining) work in this

TCD
6, 4695–4731, 2012

subject has been done based on a data set accumulated in East Antarctica (Fujita et al., 1999) using an apparatus with somewhat poorer depth resolution than employed in our measurements. Much of the discussion that follows will reference those previous publicatons.

With ϵ the dielectric constant, f the frequency of radar being employed, σ the conductivity of an acid layer and δ the difference in either ϵ or σ across some boundary, the magnitude of density (or acid) reflected power typically varies as the square of those differences, i.e. δ_ϵ^2 (or $\delta_\sigma/f)^2$ (Paren, 1981). Since both δ_ϵ and δ_σ are approximately independent of frequency in the $\sim$ MHz radio frequency regime, we expect density scattering to be independent of frequency, and conductivity scattering to vary inversely as frequency (with some temperature dependence, as well). Acid vs. density layering can be discriminated on the basis of their depth: density contrasts tend to diminish with over-pressure, and should be largely unobservable below $r \sim 1$ km depth (Fujita et al., 2000). In contrast to typically "thin" conductive and/or density contrast layers which are associated with "isochrones" (i.e, signals with timescales smaller than the experimental resolution) and therefore have signal durations that are intrinsically sub-ns scale, ice core analysis indicates that reorientation of the crystal fabric (i.e. COF scattering) typically occurs over tens of meters of ice thickness (Siegert and Kwok, 2000), corresponding to hundreds of nanoseconds in echo duration.

Additionally, continuous "volumetric" scattering (due, e.g. to air bubbles trapped in the upper, unenclathrated ice with size much smaller than typical radio wavelengths) results in weak radar returns with a wavelength dependence on amplitude $A \propto 1/\lambda^4$. This volume scattering sets the baseline above which stronger returns from planar reflections ($A \propto 1/r$) may be visible. For the case where the scattering size is much greater than one wavelength, phase coherence across the scatterers is lost, and the amplitude decreases as $1/r^2$.

TCD
6, 4695–4731, 2012

1.1 Birefringence

The presence of a preferred crystal orientation fabric can lead to an asymmetry in the radio wavespeed with azimuthal polarization; i.e. birefringence. Physically, this corresponds to a difference δ in the real permittivity ϵ' for propagation along the ordinary- vs. extraordinary-axes. In the simplest picture of two-dimensional ice crystals stacking in the horizontal plane, with the perpendicular ($\hat{c}$-axis) correspondingly aligned with the vertical $\hat{z}$-axis, one would expect radio wave propagation along the vertical from the surface to the bedrock (i.e. with the electric-field polarization axis in the horizontal) to be independent of azimuth, and birefringence to be noticeable as a difference between horizontal vs. vertical signal propagation. Laboratory measurements, in fact, determined an asymmetry of $\sim 3.3\,\%$ between these two wave speeds (Fujita et al., 1996). The local horizontal ice flow, however, produces an azimuthal asymmetry in the horizontal plane, and also suggests a "natural" axis which may result in a wavespeed asymmetry.

Although birefringence is now well-established in the ice sheet (Table 1), data on exactly what depths birefringence is physically generated within the ice sheet is still incomplete. Data indicating correlations of birefringent effects with local ice flow are also not entirely concordant; at least one measurement found a lack of alignment between the implied birefringent basis and the surface ice flow direction (Doake, 1981; Woodruff and Doake, 1979).

2 Measured azimuthal variation of radar echoes, normal incidence

2.1 Set-up

The Martin A. Pomerantz Observatory (MAPO) building, located within 1 km of the geographic South Pole, houses the signal generator and data acquisition system used for these measurements. Two 1.25-cm thick LMR-500 coaxial cables, each approximately

TCD
6, 4695–4731, 2012

25 m long, were fed from within MAPO through a conduit at the bottom of the building and out onto the snow. Each cable was then connected to a Transverse ElectroMagnetic (TEM) horn antenna on the snow surface. These antennas, constructed at the Institute of Nuclear Research in Moscow, were also used in our previous measurement of the ice attenuation length at the South Pole (Barwick et al., 2005). As with our previous measurement, for in-ice transmission, each horn antenna is placed face-down on the surface looking into the snow. These antennas have reasonably good transmission characteristics, from 60 MHz up to 1300 MHz, as indicated by the Voltage Standing Wave Ratio (VSWR) data in Fig. 1. We note that the measured frequency response shown in Fig. 1 corresponds to the horn antennas in their experimental configuration and therefore should correctly represent the horn characteristics relevant to this measurement. The forward gain of the horns is approximately 10× that of an isotropic emitter (∼ 10 dBi) in air, or ∼ 12–15 dBi in-ice. The co-polarization to cross-polarization isolation ("polarization purity") was measured at South Pole, and also in the lab at the University of Kansas, to exceed 10 dB.

Signals were taken from a fast pulse generator inside MAPO through the coaxial cable out to the transmitter horn. Receiver horn signals are high- and low-pass filtered to remove components below 200 MHz and above 1 GHz, notch filtered to suppress the large South Pole background noise at 450 MHz which serves as the station Land Mobile Radio carrier, and finally amplified by +52 dB prior to data acquisition and storage; the total time delay through the associated cables has been measured to be 190 ns. Data acquisition of receiver horn waveforms was performed using a LeCroy 950 Waverunner digital oscilloscope. This scope features adequate bandwidth (1 GHz) and a high maximum digitization speed (16 GigaSamples s^{-1} – GSa s^{-1}). For the measurements described herein, the scope sampling rate was generally set to 2 GSa s^{-1}. To enhance signal-to-noise, many waveforms (40 000 typically) were averaged. Trigger stability was ensured by splitting the output of the pulse generator, with one copy being sent to the transmitter horn antenna, and the other providing the trigger signal for the LeCroy scope.

TCD
6, 4695–4731, 2012

We note three primary differences between our radio echo sounding (RES) apparatus, which was originally developed for application in Antarctica cosmic ray detection, and that typically employed for RES measurements:

1. We use a nanosecond-scale transmitted pulse, vs. "tone" signals of frequency $\sim$ 100–200 MHz, having duration of order microseconds.
2. Our receiver data acquisition samples at between 1 and 2 GSa s^{-1}, vs. sampling rates which are comparable to the CW signal being broadcast.
3. Reflections are reconstructed directly by averaging, rather than synthesizing the reflected echogram image using SAR techniques.

2.2 Experimental results

2.2.1 Full azimuthal scan

Figures 2 and 3 display the measured voltage as a function of echo time, as the polarization orientation of the transmitter and receiver are rotated. For ease of display, echograms have been vertically offset and alternately displaced by ±100 ns relative to each other. In actuality, the most prominent echoes are observed to be synchronous within one nanosecond of each other, up to 19 µs echo time, and thus excludes the possibility of a birefringent effect in the upper half of the ice sheet, in contrast to the East Antarctica measurements (Fujita et al., 2003, 2006). Antennas aligned with MAPO were assigned a zero-degree orientation; for reference, the surface ice flows in a direction corresponding to roughly +153° in these coordinates. In these figures, the notation "A × B" designates the azimuthal polarization orientation of transmitter ("A") and receiver ("B"), respectively. "60 × 150" correspondingly indicates a cross-polarization orientation.

Several features are immediately evident from Figs. 2 and 3: (a) the presence of several short-duration returns at approximately 6, 9.6, 13.9, 17 and 19 µs with comparable shapes, (b) for the first observed echo at 6 µs, we observe apparently larger

TCD
6, 4695–4731, 2012

received power in the cross-polarization orientation than the co-polarization orientation, (c) in general, the "continuum" received power, away from evident peaks, in the cross-polarization orientation is smaller than the co-polarization power (presumably related to the geometric characteristics of volumetric scattering in the bulk ice), and (d) for the 9.6 µs echo, we observe a sequence of three distinct echoes, separated by approximately 0.1 µs. We note that the implied depth of the return at 13.9 µs is consistent with layering identified using a laser dust logger in boreholes drilled for the IceCube experiment (Abassi et al., 2012).

2.3 Time domain characteristics of observed returns

We have investigated the temporal and frequency characteristics of our observed echoes. An earlier study concluded that "anisotropic scattering", occuring at depths where the alignment of the ice crystal fabric changes directions, is responsible for many of the echoes observed at intermediate depths. Such scattering, of the COF type, should be independent of frequency, over the interval 60–179 MHz (Matsuoka et al., 2003). COF scattering can thus be distinguished from acid layer scattering, which features amplitude believed to vary inversely as frequency, but not from density layer scattering.

Figure 4 compares zooms of the time domain waveforms of the reflections observed at 6, 9.6, 13.9, 17 and 19 µs. We observe that the shallower time-domain returns are, if anything, longer in duration than the deeper returns, indicating higher fractional signal content at lower frequencies. Overall, the similarity of the waveforms suggest that the same scattering mechanism may be responsible for all observed reflections. Note that the waveforms shapes, qualitatively, disfavor a model wherein ice attenuation increases with frequency, as this would tend to reduce the sharpness of the later, rather than earlier returns.

Figures 5 and 6 show the time domain voltage magnitude, after applying software filters of $f < 500$ MHz and $f > 500$ MHz, respectively, and transforming back into the time domain. We observe greater fractional high-frequency power for the 9.6 µs return

TCD
6, 4695–4731, 2012

compared to the 6 µs reflection, consistent with the qualitative conclusion drawn from the time domain waveforms shown in Fig. 4.

2.4 Attenuation length dependence on depth and temperature

The observed echo amplitudes shown in Fig. 4 are largely determined by three factors: the intrinsic reflectivity of each layer, the diminution of signal power P_{signal} with distance, and attenuation of the signal due to continuous ice absorption. For the directional horn antennas used in this experiment, $P_{\text{signal}} \propto r^{-\alpha}$, with $1 < \alpha < 2$. If we assume that the scattering mechanisms for all reflections are the same, and further assume approximately equivalent reflection coefficients for all internal layers, we can determine a "local" amplitude attenuation length between the first three, and last three layers, as shown in Table 2, by direct application of the Friis equation (Balanis, 1997). For this calculation, we take $\alpha = 2$; assuming a cylindrical-flux tube with no transverse spreading ($\alpha = 1$) gives values approximately 20 % smaller than those presented in Table 2. Our estimates, showing a general trend of shorter attenuation lengths closer to the bed, are consistent with the expected warming of the ice sheet from below, and the corresponding reduction in attenuation length with increasing temperature. We note that the temperature dependence of conductivity scattering would lead to a reduction in reflection coefficient with depth and could therefore also account for some of the variation observed; in Table 2, we neglect the 6 °K difference in layer temperature between the depth implied for the 13.9 µs reflection vs. the 19.6 µs reflection. For this translation, we use a temperature-weighted average EM wave velocity of $169 \pm 0.3\,\text{m}\,\mu\text{s}^{-1}$ below the firn (Dowdeswell and Evans, 2004); through the firn, we use direct measurements of radio propagation wavespeed (Kravchenko et al., 2005).

2.5 Variation in return amplitude with azimuth

A comparison of the maximum amplitudes observed for the 5 primary reflections is presented in Table 3; asterisks indicate that the reflection at that depth and orientation

TCD
6, 4695–4731, 2012

angle was insufficiently distinct from noise. Figure 7 displays the peak amplitude voltages vs. co-polarization orientation angle. For three of these layers, we observe an apparent co-sinusoidal variation which is roughly in phase with the ice flow direction (153°, shown as the blue arrow in the figure); no obvious correlation is apparent for the 6 µs and 19 µs reflections. We emphasize that the azimuthal variation observed in this experiment is otherwise unrelated to the azimuthal variation reported in East Antarctica (Fujita et al., 2006); in particular, those variations were attributed to destructive interference between projections of the radio-frequency electric field vector propagating along two orthogonal axes. In our case, there is no (obvious) operative interference mechanism. I.e. the synchronousness (to within 1 nanosecond) of the reflections, at all polarizations, rules out the possibility that the observed azimuthal amplitude variation is the result of birefringence-induced interference effects; the mechanism responsible for our observed variation is therefore different than the mechanism responsible for the variations in amplitude observed at Dome Fuji, which were attributed to birefringence, and also exhibited a faster phase variation than we observe.

A previous paper (Besson et al., 2010) investigated the basal echo times at South Pole as a function of polarization. That study demonstrated that reflections through the full ice sheet, off the bedrock, do exhibit the azimuthal dependence of echo times and voltages characteristic of birefringence. Specifically, for polarizations aligned parallel to the putative ordinary axis, only one return is observed, with a voltage $V_{\mathrm{fast}}^{\mathrm{max}}$ and a negative echo time offset relative to that observed for polarizations aligned with the putative extraordinary axis, presumably rotated by $\pi/2$ radians. If we designate the voltage observed for alignments parallel to the ordinary axis as $V_{\mathrm{fast}}^{\mathrm{max}}$, then, for polarizations at $\pi/4$ radians relative to each axis, two returns should be observed, each with amplitude $1/\sqrt{2}$ as large as the co-aligned case; i.e. $V_{\mathrm{fast}}(\pi/4)/V_{\mathrm{slow}}(\pi/4) = 1$. Additionally, for this case, $V_{\mathrm{fast}}/V_{\mathrm{slow}} = V_{\mathrm{fast}}^{\mathrm{max}}/\sqrt{2}$. $V_{\mathrm{fast}}/V_{\mathrm{slow}}$ (Fig. 8, Besson et al., 2010) shows measurements consistent with these expectations, and thus, a correlation consistent with ice flow direction defining the extraordinary axis.

TCD
6, 4695–4731, 2012

3 Oblique radio wave scattering

The problem of securing power sources for both transmitters and receivers at remote field sites presents an obstacle to performing radar measurements at non-zero inclination angles. Nevertheless, such measurements are the most obvious method of probing the three-dimensional characteristics of birefringence, rather than merely investigating effects exclusively in the horizontal plane.

In our picture, a ray having an electric-field polarization vector $\boldsymbol{E}$ incident on a medium (in our case, ice) is characterized by three principal orthogonal axes x, y and z, which we associate with the ice-flow direction (y-), the vertical (z-) and a corresponding x-axis given by the cross-product of y- and z-unit vectors. For our geometry, y- is approximately grid south, and x- is approximately grid east.

In the general case of three-dimensional birefringence, we associate the three coordinate axes with corresponding refractive-indices n_x, n_y and n_z. Using the angles θ and ϕ as the conventional polar and azimuthal angles, the amplitudes of the projected components are then given by the standard expressions: $A_x = |\boldsymbol{E}| \sin\theta \cos\phi$, $A_y = |\boldsymbol{E}| \sin\theta \sin\phi$, and $A_z = |\boldsymbol{E}| \cos\theta$. At South Pole, such measurements were performed in December 2011, both along and transverse to the horizontal ice-flow direction (Fig. 9). Both transmitter and receiver were propped up approximately 1 m above the ice surface, at a 45-degree angle relative to the surface, thus broadcasting both a direct signal through the air, as well as a signal broadcast into, and received after reflection from the intervening ice. The ray geometry for typical measurements are shown in Fig. 10.

A simple trigger, based on reception of the direct through-air signal broadcast at the receiver was employed – a more sophisticated trigger, which would have synched the received signal to a simultaneously-broadcast, narrow-band transmitter signal as was done in the past (Barwick et al., 2005), was, unfortunately, not available for these measurements. At each transmitter location, both horizontally polarized ("HPol") and also vertically polarized ("VPol") data were collected. An additional data point was taken

TCD
6, 4695–4731, 2012

approximately 60 degrees relative to the ice flow direction (i.e. 30 degrees relative to a perpendicular to the ice flow direction and labeled "Tx3" in the figure) at a transmitter-receiver separation of 400 m as a cross-check.

Our primary results are shown in Figs. 11 and 12. A cross-correlation analysis determines the time staggers between the two signal onsets to be 49.2 ns and 50.1 ns in Figs. 11 and 12, very consistent with the 50.0 ns time offset previously reported for the birefringent propagation time asymmetry measured in vertical propagation (Besson et al., 2010), as expected from Fig. 10. As a cross-check, propagation from "Tx3" also yields an echo time difference consistent with 50 ns (Fig. 13).

In principle, the VPol signals can be projected separately into the horizontal and vertical planes. However, the amplitude of the VPol component, given the relatively short horizontal baselines, is immeasurably small in our data sample. Clearly, what is needed to make this measurement more compelling is to broadcast over larger horizontal distances, and thereby probe a more vertical VPol propagation vector. Such a measurement will require a revised trigger scheme, such as that used previously at South Pole (Barwick et al., 2005).

3.1 Ice depth measurement

The times of the received bedrock echoes relative to the through-air trigger, for each polarization, are directly given by the average index-of-refraction and the depth of the intervening ice. Antarctic aerial surveys, such as BEDMAP and CRESIS, have provided a great service to the community by providing detailed tables of their calculated depth over the Antarctic continent. (In what follows, we use the BEDMAP data available in 2011; those data are currently being superceded by the BEDMAP-2 depth analysis.) Those depth values are obtained using monochromatic radio signals of order 10 µs in duration, and coherently adding many echograms. To estimate the precision of those surveys, we can simply compare the tabulated depths for the two surveys, at common sampling locations. The latitude and longitude of common sampling points, defined as points common to both surveys that are tabulated as being within 50 m of each other

TCD
6, 4695–4731, 2012

along the Antarctic surface, are shown in Fig. 14. The ice thickness difference, at those locations, as a function of the numerical separation (in meters) between the CRESIS vs. the BEDMAP sampling points, is shown in Fig. 15. Although the depth difference distribution clusters at zero, we observe large deviations from zero depth difference; the rms of the distribution is approximately 115 m.

We can estimate the ice thickness depth at South Pole from our data, obtained using a considerably faster pulse, using the following procedure. Since the index-of-refraction of refraction varies through the firn, we calculate an "average" value based on the measured radiofrequency light speed to a depth of 200 m (Kravchenko et al., 2005), and assuming a constant value of $n = 1.782$ at greater depths; this procedure yields a depth-averaged index-of-refraction value of 1.773. We can then calculate the ice depth, independent of any system delays, by comparing the measured through-ice transit time, relative to the through-air trigger signal, against the calculated through-ice transit time, knowing the horizontal spacing between transmitter and receiver at each source point, and leaving the depth as a free parameter. Results are shown in Fig. 16. We find relatively good agreement between the average of our three measurements (2841 ± 15 m) with a previous estimate of 2850 m for the ice thickness at South Pole (Besson et al., 2010). Note that the errors are comparable to the expected depth difference due to bedrock slope. By comparison, we note that the BEDMAP (The BEDMAP Collaboration, 2012) collaboration have tabulated the ice sheet depths at latitude 89.975° S, in increments of 0.36 degrees of longitude. Those depths are shown in polar form, with an offset of 2700 m, in Fig. 17. Our value is bracketed by the tabulated BEDMAP depths, albeit with smaller error bars.

3.2 Future work using embedded transmitters

Owing to the difficulty of embedding transmitters at depth within the ice sheet itself, virtually all of the radar data that has been collected thus far has been collected along a vertical chord. In January 2011, three high-power (5 kV amplitude, 100 ps rise time) radio pulsers were deployed as part of the Askaryan Radio Array (ARA, Allison, 2011)

TCD
6, 4695–4731, 2012

deployment during that austral season. Two have been frozen in at depths of 1450 m (offset horizontally by approx. 200 m); the third has been frozen in at a depth of 2400 m. These pulsers are locally slaved to a high-precision Rubidium oscillator, also deployed in-ice at the location of the transmitters themselves, to permit waveform averaging of received signals by either embedded, or surface receivers. Those transmitters should afford an unprecedented opportunity to measure the complex permittivity of ice, in the radio frequency range, and provide a new suite of measurements, not only for the ARA particle astrophysics experiment, but the radioglaciological community as well. In particular, those transmitters will allow high-precision, long-baseline probes of the ice along a horizontal chord for the first time.

4 Conclusions

We have observed azimuthal correlations of echo returns with ice flow direction at South Pole, which we summarize as follows:

- As with previous work around Dome Fuji, we also observe a correlation of surface iceflow direction with echo amplitude for internal reflections at echo times up to 20 µs. However, we note several differences between our measurements and those previous probes of the ice sheet in East Antarctica (Fujita et al., 2006):
  - Although reflections at ∼1 km depth in East Antarctica were explained as due to transitions between layers with different COF alignments, we find no evidence for the expected concommitant birefringent effect due to COF alignment. This implies that the ice fabric is not monolithic across the Antarctic continental surface.
  - For some alignments, we observe cross-polarized signal strength that exceeds the co-polarized signal strength, in contrast to the expectation (Fujita et al., 2003) that the co-polarized signal sets a physical limit on the observed cross-polarized signal strength. Such an effect is familiar from the application

TCD
6, 4695–4731, 2012

of successively rotated diffraction gratings in optics, and suggests that such a mechanism may be operative within the ice, as well, with layers functioning as gratings.

- A separate data sample taken in December 2011, with transmitter and receiver separated horizontally by ≈ 0.5 km affirms the quantitative results of our previous measurements for the total birefringent asymmetry through a vertical chord of the ice, using co-located transmitter and receiver. Our measurements also permit a precise measurement of the thickness of the ice sheet at Pole (2841 ± 15 m), where the quoted error is based on the observed spread in our individual trials.
- In the "standard" picture, if the c-axis is exactly vertical, and the wavespeed asymmetry is different only for propagation perpendicular (i.e. along z) vs. perpendicular (horizontal) to the crystal stacking axis (i.e. $\hat{c}$), then the wavespeed is uniform for all directions in the horizontal plane and there is no expected birefringence as a function of azimuthal orientation. However, our results imply an asymmetry for azimuthal propagation along vs. perpendicular to the ice flow direction, in contrast to the laboratory measurements for single crystals, which would have implied azimuthal symmetry. Our results *are* consistent with a vertical girdle average orientation at depths greater than ∼ 1200 m, although ice core analysis indicates that the ice should be increasingly uniaxial at these depths.

Two additional inputs could significantly clarify the association between Radar Echo Sounding measurements and ice chemistry, either: (1) an ice core taken at South Pole, preferably retaining the azimuthal information of the extracted core itself, or (2) ns-duration probes of the Antarctic ice sheet at a location where a core has already been taken (Vostok, or WAIS, e.g.). Such data will hopefully be available at some point in the near future.

Acknowledgements. The authors particular thank Chris Allen and John Paden (University of Kansas), John Ralston (University of Kansas), Rebecca Boon (Pennsylvania State University), Joe MacGregor (University of Texas), and Kenny Matsuoka (Norwegian Polar Institute)

TCD
6, 4695–4731, 2012

for very helpful discussions, as well as our colleagues on the RICE and ANITA experiments. We also thank Andy Bricker of Lawrence High School (Lawrence, KS) for his assistance working with Lawrence High School students who performed essential antenna calibrations. This work was supported by the National Science Foundation's Office of Polar Programs (grant OPP-0826747) and QuarkNet programs. Any opinions, findings, and conclusions or recommendations expressed in this material are those of the author(s) and do not necessarily reflect the views of the National Science Foundation.

References

Abassi, R., et al.: South Pole glacial climate record from borehole laser particulate stratigraphy, J. Glaciol., submitted, 2012. 4701

Allison, P., Auffenberg, J., Bard, R., Beatty, J. J., Besson, D. Z., Boeser, S., Chen, C., Chen, P., Connolly, A., Davies, J., DuVernois, M., Fox, B., Gorham, P. W., Grashorn, E. W., Hanson, K., Haugen, J., Helbing, K., Hill, B., Hoffman, K. D., Huang, M., Huang, M. H. A., Ishihara, A., Karle, A., Kennedy, D., Landsman, H., Laundrie, A., Liu, T. C., Macchiarulo, L., Mase, K., Meures, T., Meyhandan, R., Miki, C., Morse, R., Newcomb, M., Nichol, R. J., Ratzlaff, K., Richman, M., Ritter, L., Rotter, B., Sandstrom, P., Seckel, D., Touart, J., Varner, G. S., Wang, M.-Z., Weaver, C., Wendorff, A., Yoshida, S., and Young, R.: Design and initial performance of the Askaryan Radio Array prototype EeV neutrino detector at the South Pole, Astropart. Phys., 35, 457–477, 2011. 4706

Balanis, C.: Antenna Theory, Analysis and Design, J. Wiley and Sons, New York City, NY, 1997. 4702

Barwick, S., Besson, D., Gorham, P., and Saltzberg, D.: South Polar in situ radio frequency ice attenuation, J. Glaciol., 51, 231–238, 2005. 4699, 4704, 4705

BEDMAP: British Antarctic Survey, available at: http://www.antarctica.ac.uk/bedmap/ (last access: November 2012), 2012. 4706, 4728

Besson, D. Z., Jenkins, J.,Matsuno, S., Nam, J., Smith, M., Barwick, S. W., Beatty, J. J., Binns, W. R., Chen, C., Chen, P., Clem, J. M., Connolly, A., Dowkontt, P. F., DuVernois, M. A., Field, R. C., Goldstein, D., Gorham, P. W., Goodhue, A., Hast, C., Hebert, C. L., Hoover, S., Israel, M. H., Kowalski, J., Learned, J. G., Liewer, K. M., Link, J. T., Lusczek, E., Mercurio, B., Miki, C., Miočinović, P., Naudet, C. J., Ng, J., Nichol, R., Palladino, K., Reil, K., Romero-Wolf, A.,

TCD
6, 4695–4731, 2012

Rosen, M., Ruckman, L., Saltzberg, D., Seckel, D., Varner, G. S., Walz, D., and Wud, F.: In situ radioglaciological measurements near Taylor Dome, Antarctica and implications for UHE neutrino astronomy, Astropart. Phys., 29, 130–157, 2008. 4712

Besson, D., Kravchenko, I., Ramos, A., and Remmers, J.: Radio frequency birefringence in South Polar ice and implications for neutrino reconstruction, Astropart. Phys., 34, 755–768, 2010. 4703, 4705, 4706

CReSIS (Center for Remote Sensing of Ice Sheets): Antarctic Data website, available at: ftp://data.cresis.ku.edu/data/kuband/2011_Antarctica_DC8/ (last access: November 2012), 2010a. 4728

CReSIS (Center for Remote Sensing of Ice Sheets): Greenland Data website, available at: ftp://data.cresis.ku.edu/data/kuband/2011_Greenland_P3/ (last access: November 2012), 2010b. 4728

Doake, C. S. M.: Polarization of radio waves propagated through George VI ice shelf, Brit. Antarct. Surv. B., 56, 1–6, 1981. 4698

Doake, C., Corr, H., and Jenkins, A.: Polarization of radio waves transmitted through Antarctic ice shelves, Ann. Glaciol., 34, 165–170, 2002. 4712

Doake, C., Corr, H., Jenkins, A., Nichols, K., and Stewart, C.: Applications of SAR polarimetry and polarimetric interferometry, Euro. Space Agency, 529, 313–320, 2003. 4712

Dowdeswell, J. A. and Evans, S.: Investigations of the form and flow of ice sheets and glaciers using radio-echo sounding, Rep. Prog. Phys., 67, 1821–1863, 2004. 4702

Drews, R., Eisen, O., Weikusat, I., Kipfstuhl, S., Lambrecht, A., Steinhage, D., Wilhelms, F., and Miller, H.: Layer disturbances and the radio-echo free zone in ice sheets, The Cryosphere, 3, 195–203, doi:10.5194/tc-3-195-2009, 2009. 4696

Fujita, S. and Mae, S.: Relation between ice sheet internal radio-echo reflections at Mizuho Station, Antarctica, Ann. Glaciol., 17, 269–275, 1993.

Fujita, S., Matsuoka, T., Morishima, S., and Mae, S.: The measurement on the dielectric properties of ice at HF, VHF and microwave frequencies, Geoscience and Remote Sensing Symposium, IGARSS '93, Abstract #48, 3, 1258–1260, 1993. 4698, 4712

Fujita, S., Maeno, H., Uratsuka, S., Furukawa, T., Mae, S., Fujii, Y., and Watanabe, O.: Nature of radio echo layering in the Antarctic ice sheet detected by a two-frequency experiment, J. Geophys. Res., 104, p. 13013, doi:10.1029/1999JB900034, 1999. 4697

Fujita, S., Matsuoka, T., Ishida, T., Matsuoka, K., and Mae, S.: A summary of the complex dielectric permittivity of ice in the megahertz range and its application for radar sounding of

TCD
6, 4695–4731, 2012

polar ice sheets, in: Physics of Ice Core Records, edited by: Hondoh, T., Hokkaido University Press, Sapporo, 185–212, 2000. 4697

Fujita, S., Matsuoka, K., Maeno, H., and Furukawa, T.: Scattering of VHF radio waves from within an ice sheet containing the vertical-girdle-type ice fabric and anisotropic reflection boundaries, Ann. Glaciol., 37, 305–316, 2003. 4700, 4707, 4712

Fujita, S., Maeno, H., and Matsuoka, K.: Radio-wave depolarization and scattering within ice sheets: a matrix-based model to link radar and ice-core measurements and its application, J. Glaciol., 52, 407–424, 2006. 4700, 4703, 4707, 4712

Hargreaves, N. D.: The polarization of radio signals in the radio echo sounding of ice sheets, J. Phys. D Appl. Phys., 10, 1285–1304, 1977. 4712

Hargreaves, N. D.: The radio frequency birefringence of polar ice, J. Glaciol., 21, 301–313, 1978.

Kravchenko, I., Besson, D., and Meyers, J.: In situ index of refraction measurements of the South Polar firn with the RICE detector, J. Glaciol., 50, 522–532, 2005. 4702, 4706

Matsuoka, K., Furukawa, T., Fujita, S., Maeno, N., Uratsuka, S., Naruse, R., and Watanabe, O.: Crystal orientation fabrics within the Antarctic ice sheet revealed by a multipolarization plane and dual-frequency radar survey, J. Geophys. Res., 108, 2499, doi:10.1029/2003JB002425, 2003. 4701

Matsuoka, K., Uratsuka, S., Fujita, S., and Nishio, F.: Ice-flow-induced scattering zone within the Antarctic ice sheet revealed by high-frequency airborne radar, J. Glaciol., 50, 382–388, 2004.

Matsuoka, K., Wilen, L., Hurley, S. P., and Raymond, C. F.: Effects of birefringence within ice sheets on obliquely propagating radio waves, IEEE T. Geosci. Remote, 47, 1429–1443, 2009.

Matsuoka, T., Fujita, S., Morishima, S., and Mae, S.: Precise measurement of dielectric anisotropy in ice Ih at 39 GHz, J. Appl. Phys., 81, 2344–2348, 1997. 4712

Paren, J.: Reflection coefficient at a dielectric interface, J. Glaciol., 27, 203–204, 1981. 4697

Siegert, M. J. and Kwok, R.: Ice-sheet radar layering and the development of preferred crystal orientation fabrics between Lake Vostok and Ridge B, Central East Antarctica, Earth Planet. Sci. Lett., 179, 227–235, 2000. 4697

Woodruff, A. H. and Doake, C. S. M.: Depolarization of radio waves can distinguish between floating and grounded ice sheets, J. Glaciol., 23, 223–232, 1979. 4698, 4712

TCD

6, 4695–4731, 2012

Table 1. Summary of recent birefringence measurements.

Group	Locale	$\delta_{e'}$ Result	Comment
Hargreaves (1977)	Greenland	0.024–0.031 %	
Woodruff and Doake (1979)	Bach Ice Shelf	0.52 %	
Fujita et al. (1996)	Lab Ice	(3.7 ± 0.6) %	9.7 GHz
Matsuoka et al. (1997)	Lab Ice	∼ 3.4 %	1 MHz–39 GHz
Doake et al. (2002)	Brunt Ice Shelf	> 0.14–0.47 %	
Doake et al. (2003)	George VI Ice Shelf	> 0.05–0.15 %	
Fujita et al. (2003)	Mizuho Station	measurable	
Fujita et al. (2006)	Mizuho	1.5 %–3.5 %	frequency-domain
Besson et al. (2008)	Taylor Dome	0.24 %	time-domain

TCD
6, 4695–4731, 2012

Table 2. Inter-layer attenuation lengths, calculated from amplitudes measured for returns, and assuming uniform reflectivity of all layers, as discussed in text. First column indicates first reflecting layer; successive columns indicate second reflecting layer used to calculate attenuation length via Friis equation. Estimated errors are of order 30 %.

	13.9 µs	17.2 µs	19.6 µs
6 µs	3348 m	1521 m	1514 m
9.6 µs	1170 m	867 m	964 m
13.9 µs		643 m	849 m

TCD
6, 4695–4731, 2012

Table 3. Peak voltages (in mV) for indicated reflections, as a function of angle. Asterisks indicate very low observed voltage signal : noise.

Orientation	6 µs	9.6 µs	13.9 µs	17 µs	19 µs
+270 × +00 deg	28.5	5.6	2.0	1.2	0.7*
+90 × +0 deg	31.4	5.7	1.9	0.96*	0.8
+60 × +150 deg	30.5	12.8	0.9*	0.7	0.6*
+180 deg	27.4	16.4	3.3	0.9*	1.0
+150 deg	17.9	15.9	5.1	1.0*	1.3
+120 deg	18.8	9.9	3.8	1.0*	0.9
+90 deg	21.1	6.9	1.7	1.0*	0.8*
+60 deg	14.9	5.2	1.0*	1.6*	0.8*
+30 deg	29.6	11.8	1.2*	1.3	0.8
0 deg	25.4	16.6	3.0	1.1	1.0

TCD
6, 4695–4731, 2012

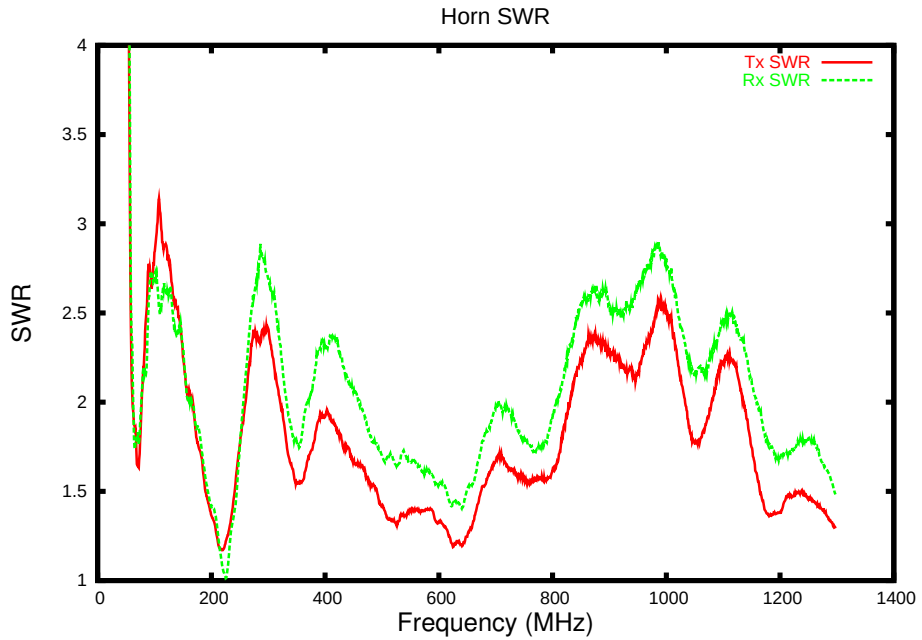

Fig. 1. Voltage Standing Wave Ratio (VSWR) for both transmitter (Tx) and receiver (Rx) horn used for data taken at South Pole.

TCD
6, 4695–4731, 2012

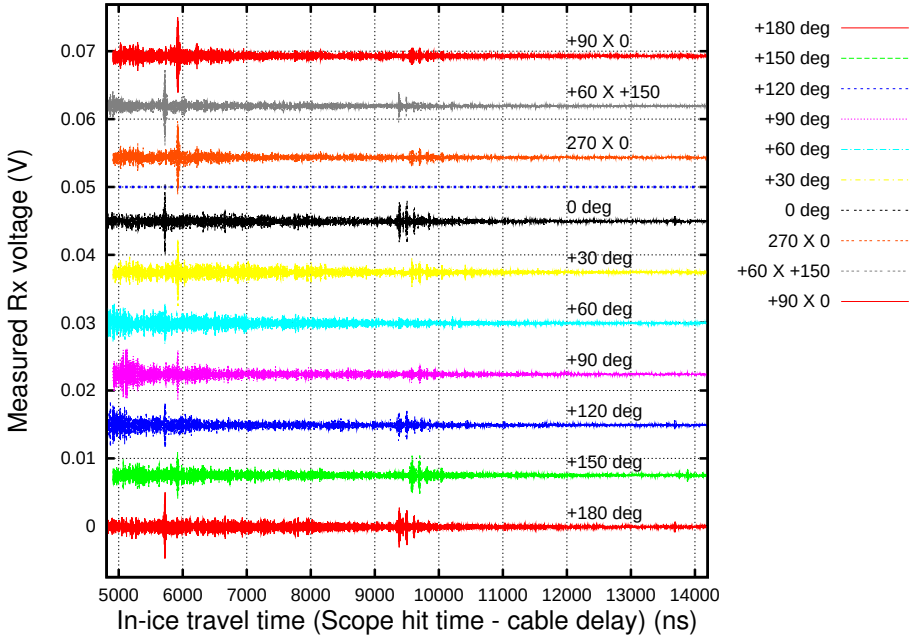

Fig. 2. Ensemble of echo amplitudes observed as a function of azimuthal orientation, for both co-polarized and cross-polarized broadcast signals, for echo times between 5 μs and 14 μs. In addition to vertical offset, alternate waveforms are also offset by ±100 ns along horizontal for visual clarity.

TCD
6, 4695–4731, 2012

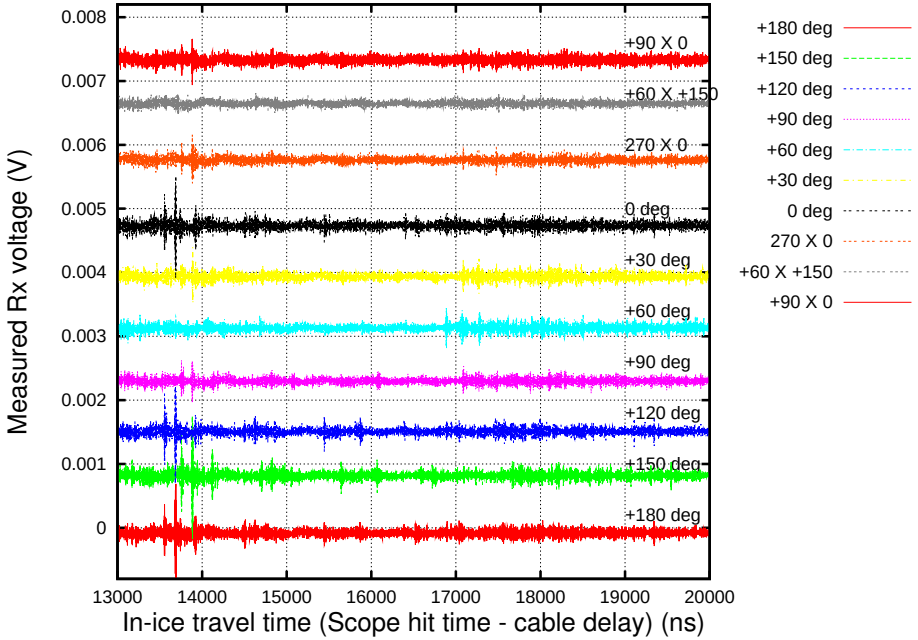

Fig. 3. Ensemble of echo amplitudes observed as a function of azimuthal orientation, for both co-polarized and cross-polarized broadcast signals, for echo times between 13 µs and 20 µs. In addition to vertical offset, alternate waveforms are also offset by ±100 ns along horizontal.

TCD
6, 4695–4731, 2012

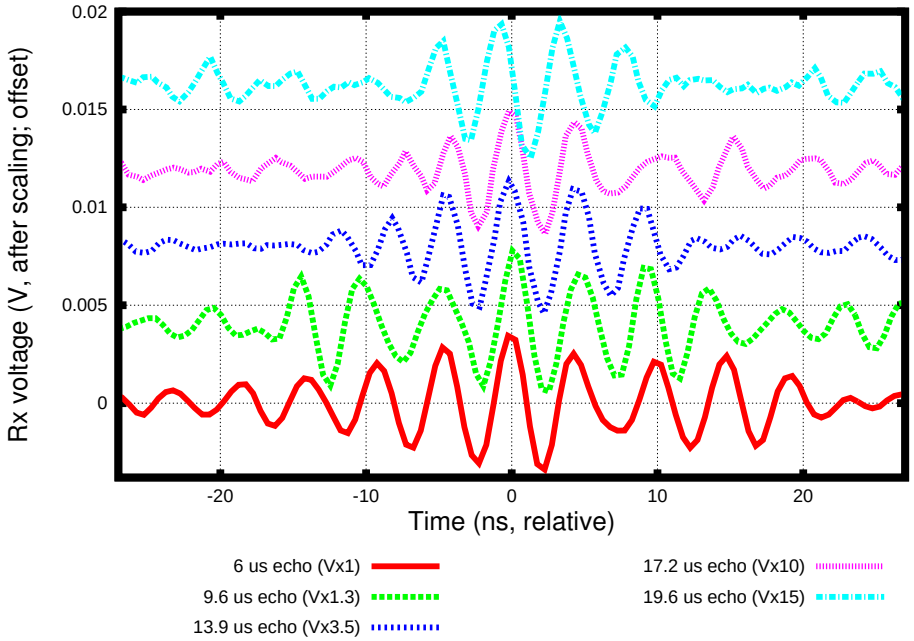

Fig. 4. Overlay of waveforms observed for various echoes. Amplitudes have been multiplied by indicated scale factors (in parenthesis) to facilitate visual comparison.

TCD
6, 4695–4731, 2012

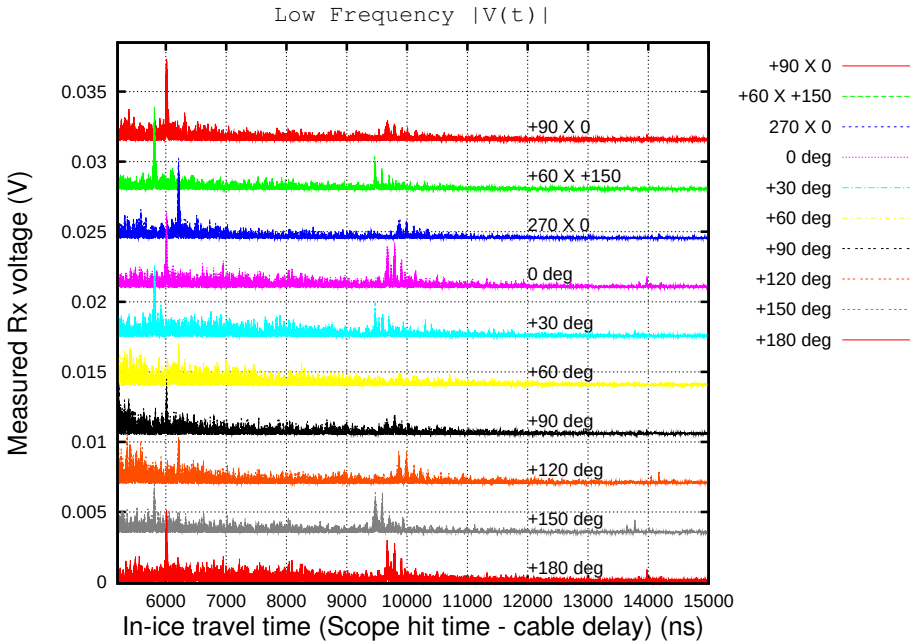

Fig. 5. Voltage magnitude after applying a 500 MHz low-pass filter to the data shown in Fig. 2.

TCD
6, 4695–4731, 2012

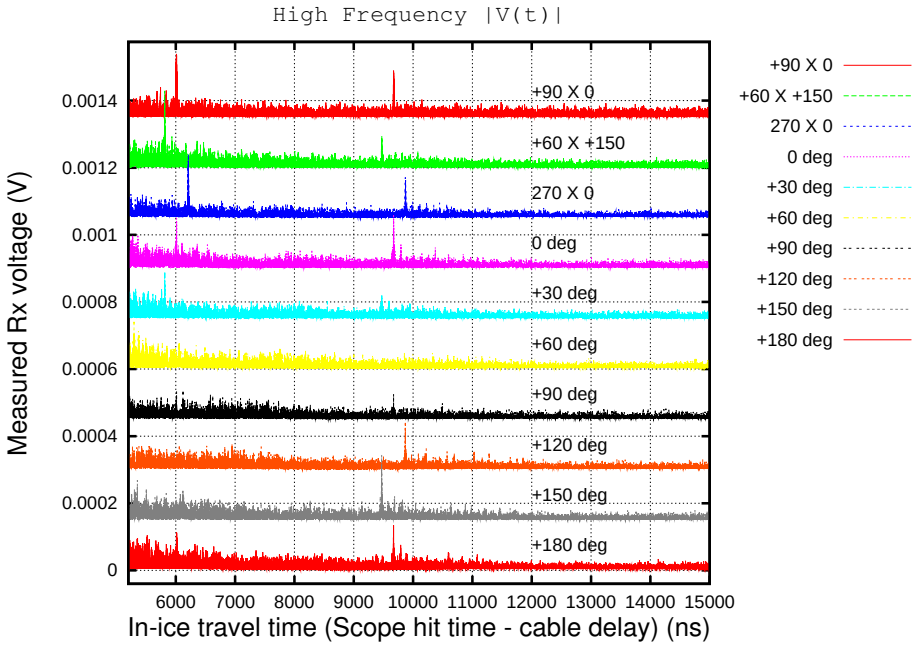

Fig. 6. Voltage magnitude after applying a 500 MHz high-pass filter to the data shown in Fig. 2.

TCD
6, 4695–4731, 2012

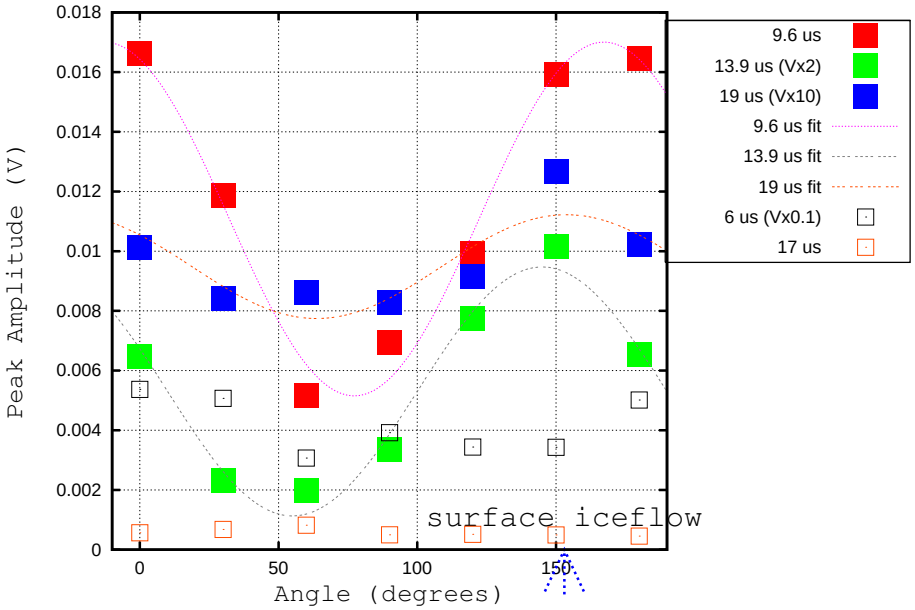

Fig. 7. Data of previous table presented in graphical form, with sinusoidal fits overlaid.

TCD
6, 4695–4731, 2012

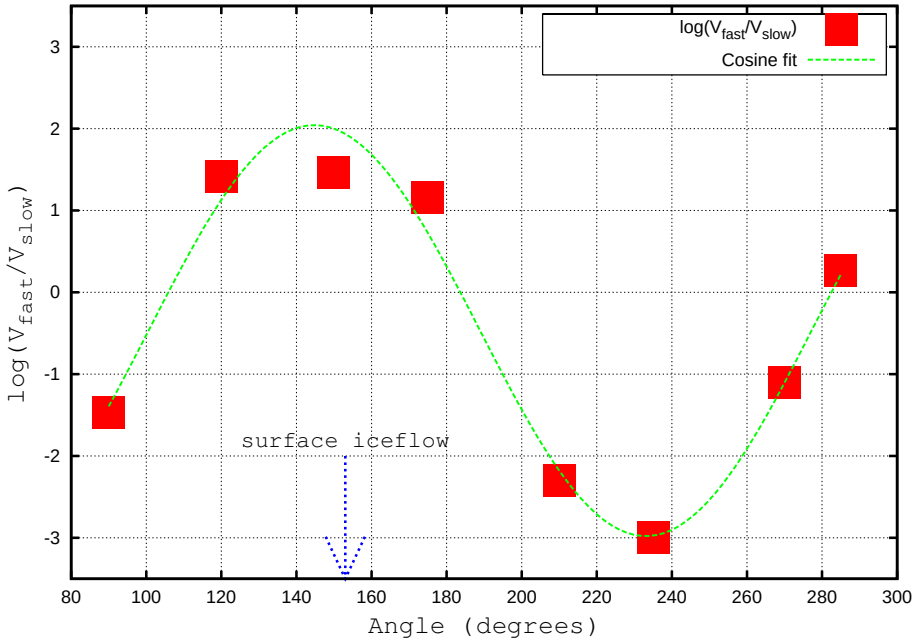

Fig. 8. Ratio of amplitudes for "fast" vs. "slow" reflection signals, as a function of azimuthal orientation of co-polarized surface horns.

TCD
6, 4695–4731, 2012

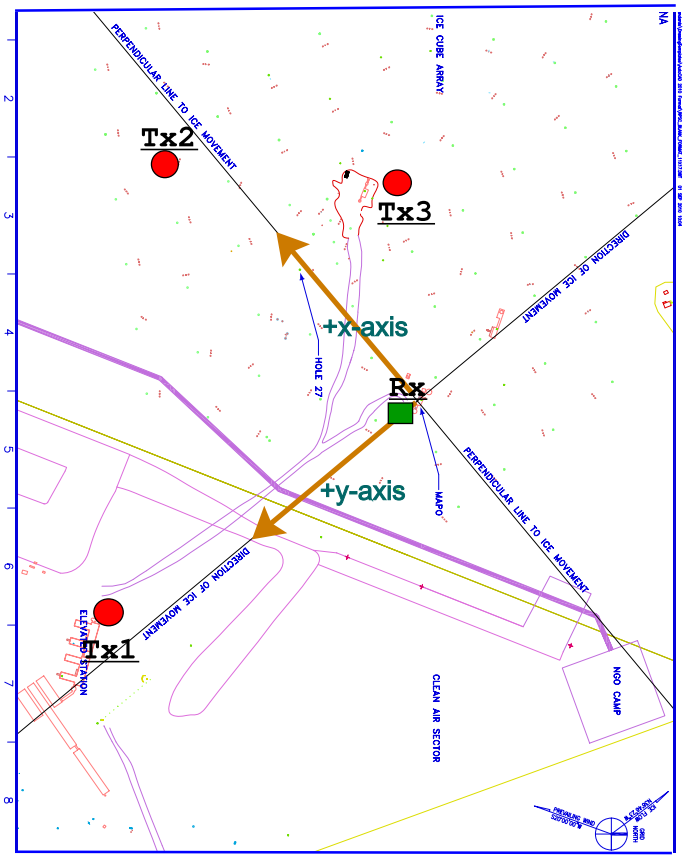

Fig. 9. Map of South Pole base, with geometry of measurement s made in December 2011 overlaid. The receiver ("Rx") is at a single location just outside of MAPO; transmitters ("Tx") were employed at three different sites, as shown. Note that location Tx1 corresponds to the location of the main South Pole Elevated Station itself. Full-scale along the horizontal is approximately 1 km.

TCD
6, 4695–4731, 2012

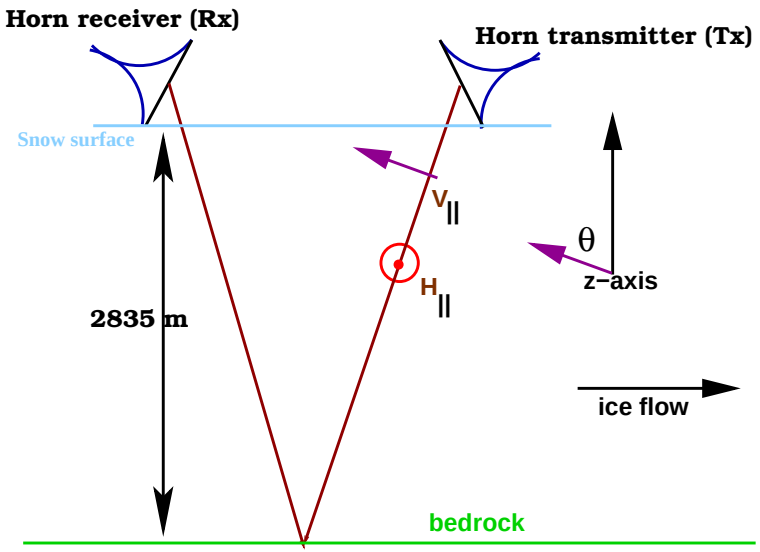

Fig. 10. Schematic of signal propagation geometry for antenna configuration parallel to the ice-flow axis; in this case, the transmitter used corresponds to "Tx1", as denoted in the previous figure. Vertical axis is defined as "+z"; the polar angle between the VPol propagation vector and the z-axis is defined as θ. Geometries for the other two transmitter positions ("Tx2" and "Tx3" in the previous figure) are not shown.

TCD
6, 4695–4731, 2012

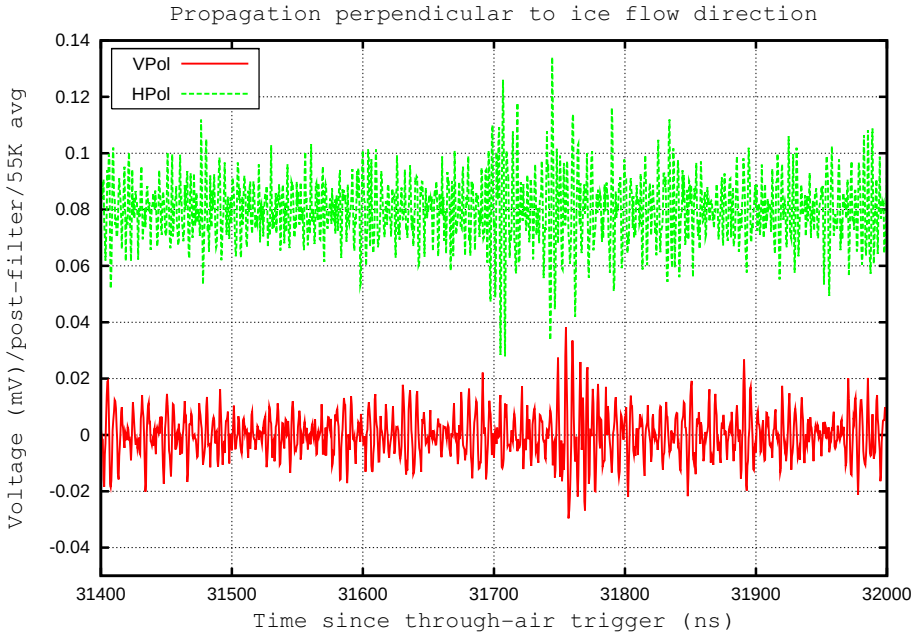

Fig. 11. Reflection echoes observed for HPol and VPol propagation; transmitter (at "Tx1") and receiver separated by ∼ 800 m and radio propagation aligned with the local ice-flow direction at South Pole. Note the suppressed zero along the x-axis, corresponding to the trigger time.

TCD
6, 4695–4731, 2012

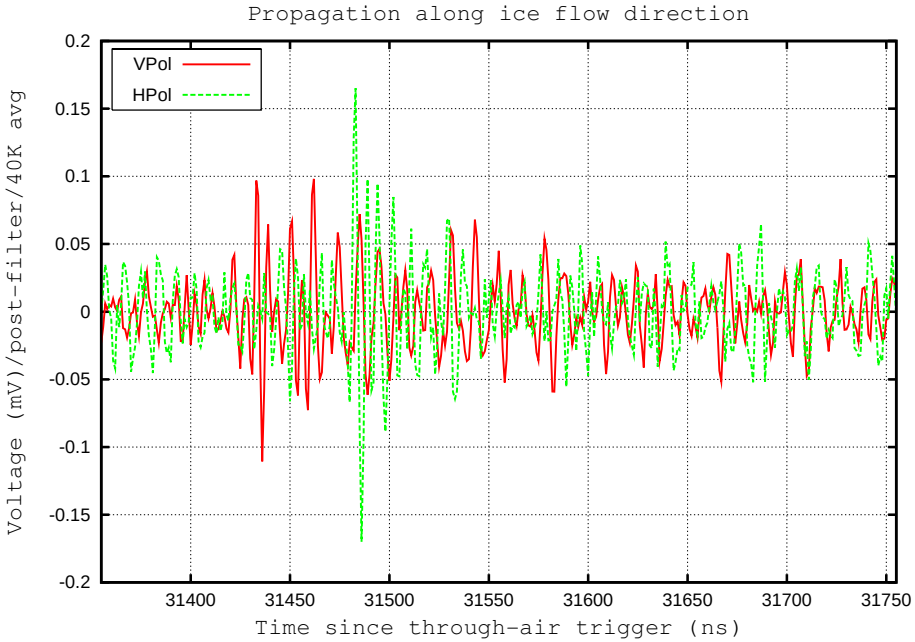

Fig. 12. Reflection echoes observed for HPol and VPol propagation; transmitter (at "Tx2") and receiver separated by ∼ 600 m and radio propagation transverse to the local ice-flow direction at South Pole.

TCD
6, 4695–4731, 2012

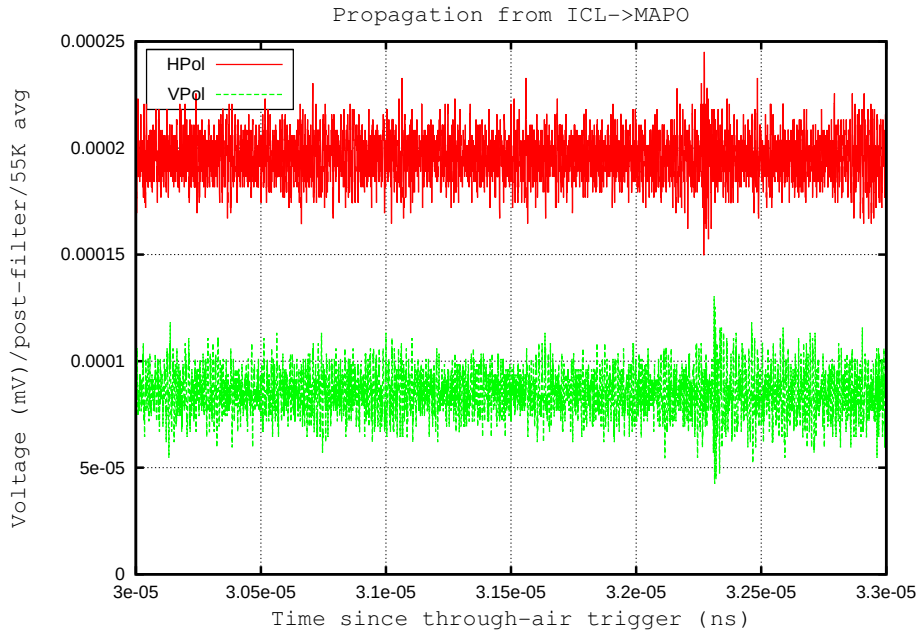

Fig. 13. Reflection echoes observed for HPol and VPol propagation; transmitter (at "Tx3") and receiver separated by ∼ 400 m and radio propagation at 60 degrees relative to the local ice-flow direction at South Pole.

TCD
6, 4695–4731, 2012

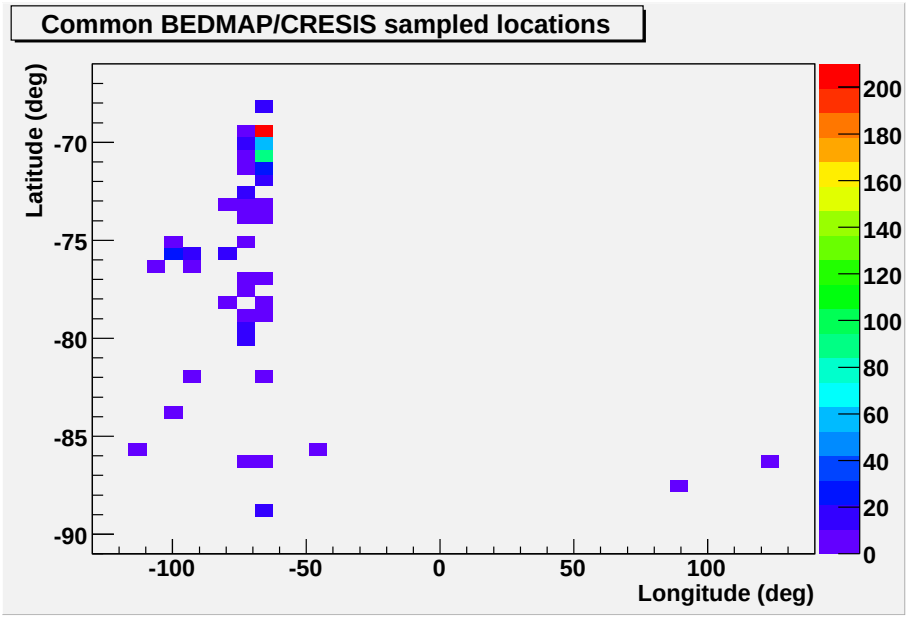

Fig. 14. Latitude/longitude of Antarctic regions for which both the CRESIS (CReSIS1, 2010; CReSIS2, 2010) and BEDMAP (The BEDMAP Collaboration, 2012) collaborations supply publicly-available ice thickness estimates.

TCD
6, 4695–4731, 2012

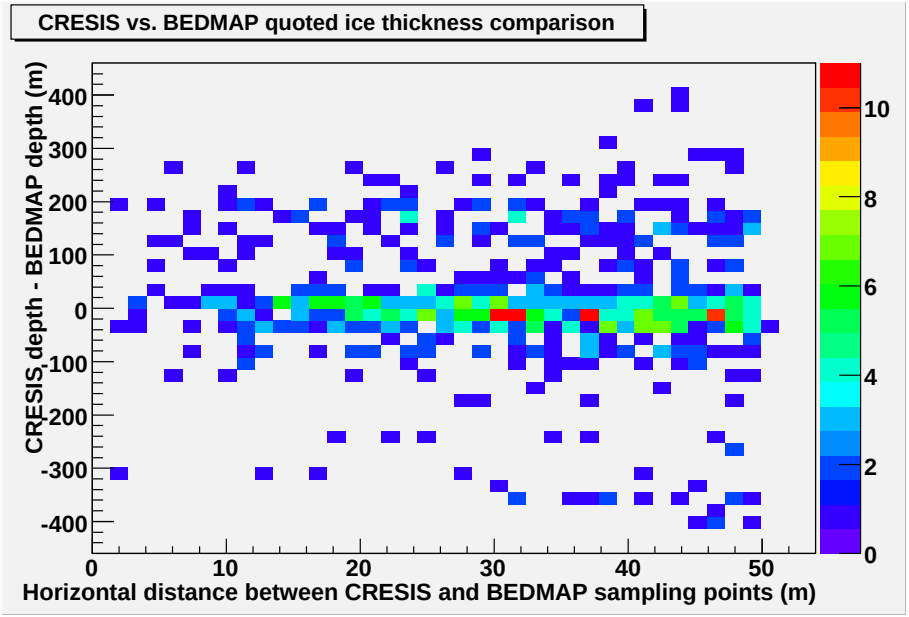

Fig. 15. Calculated ice thickness difference (m), as a function of sampling-point separation distance, at Antarctic points for which both the CRESIS and BEDMAP collaborations supply publicly-available ice thickness estimates.

TCD
6, 4695–4731, 2012

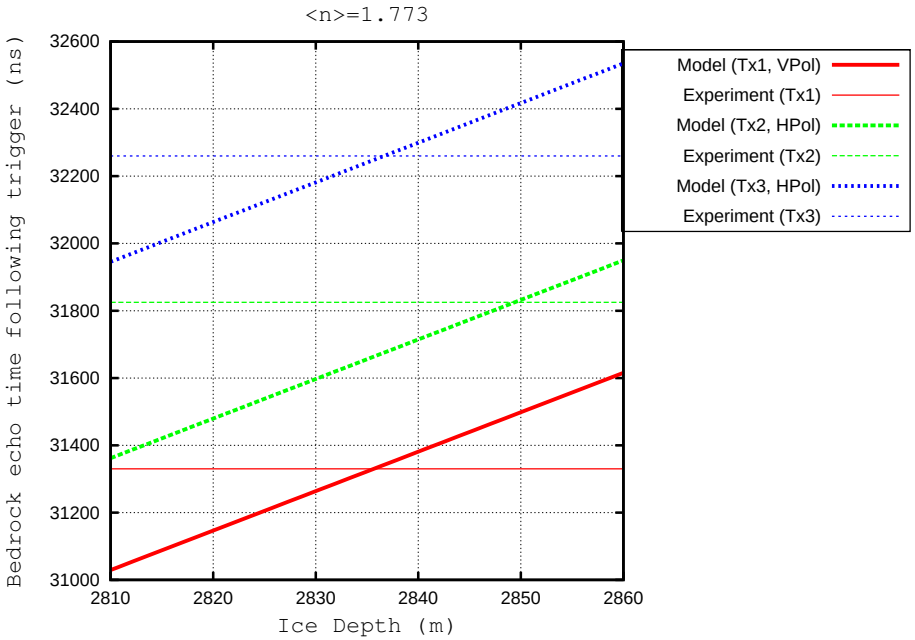

Fig. 16. Determination of ice depth at South Pole. Horizontal lines represent measured time delay between in-air vs. through-ice signal transmission from three different transmitter source locations. Slanted lines represent calculated in-ice echo delay time, as a function of ice thickness.

TCD
6, 4695–4731, 2012

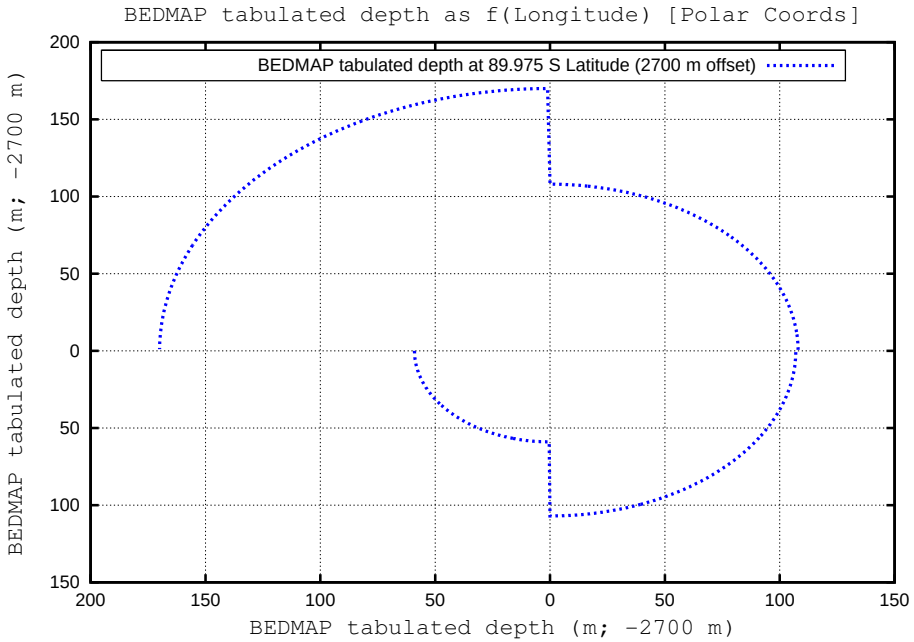

Fig. 17. Polar representation of tabulated BEDMAP depths for region around South Pole. Numbers shown include offset of 2700 m; the tabulated depths at 45, 135, −135 and −45 degrees longitude are 2808, 2870, 2759, and 2807 m, respectively. Note the discontinuities in the tabulated depths at 0, 90, 180 and −90 degrees longitude, taken to be indicative of the interpolation systematic error in the vicinity of South Pole.

TCD
6, 4695–4731, 2012